

Morphology and distribution of dolines on ultramafic rocks from airborne LiDAR data: the case of southern Grande Terre in New Caledonia (SW Pacific)

Julie Jeanpert,^{1,4*} Pierre Genthon,² Pierre Maurizot,¹ Jean-Luc Folio,³ Myriam Vendé-Leclerc,¹ Jeremy Sérino,^{1,2} Jean-Lambert Join⁴ and Marion Iseppi^{1,5,6}

¹ DIMENC/Geological Survey of New Caledonia, Nouméa, New Caledonia

² IRD/HydroSciences Montpellier, University of Montpellier, France

³ Department of Geology, Vale NC, New Caledonia

⁴ Laboratoire Géosciences Réunion – IGP – University of La Réunion, Saint-Denis, Reunion Island

⁵ BRGM New Caledonia, Nouméa, New Caledonia

⁶ University of Nouméa, Nouméa, New Caledonia

Received 17 May 2015; Revised 18 March 2016; Accepted 24 March 2016

*Correspondence to: Julie Jeanpert, DIMENC/Geological Survey of New Caledonia, 4 rue Galliéni, BP 465, Nouméa Cedex, New Caledonia. E-mail: julie.jeanpert@gouv.nc

ESPL

Earth Surface Processes and Landforms

ABSTRACT: Dolines are closed geomorphological depressions which are surface manifestations of karstic systems. Usually developed on limestones, they also typify the morphology of the New Caledonian landscape, particularly on the southern massif of the main island (known as Massif du Sud). The specificity of dolines here lies in their development on ultramafic rocks. They are evidences of subsidence, suffosion and collapse phenomena resulting from dissolution weathering of peridotites. However, extensive underground drainage systems are still not yet recognized.

Semi-automatic mapping of dolines is carried out on a 148 km² area of the Massif du Sud from a high accuracy LiDAR digital elevation model. In this area 8601 dolines ranging from 1 m² to 2 km² are identified and morphologically characterized with precision. Most are small, shallow and round-shaped, yet more complex shapes are locally observed. Size distribution analysis allows the setting of a threshold of 20 000 m² above which surface processes rather than chemical weathering control doline evolution. Doline density analysis reveals high concentrations on flat areas where ferricrete overlies the complete weathering profile, especially in the case of elevated rainy watersheds. Dolines are aligned and elongated along a north 135° ± 5° major fracture direction, which is inherited from the obduction of the Pacific Plate upper mantle in the Late Eocene.

Finally, we propose a pioneering morphometric typology of dolines that provides important clues as to pseudokarstic activity. We define collapse, bowl-shaped and flat bottom dolines. Collapse and bowl-shaped dolines are assumed to denote active pseudokarst. They may widen and deepen, or eventually be filled by sediments. They are distinguished from flat bottom dolines that are partially to completely filled, which suggests that they are associated with paleo-pseudokarsts. However the groundwater flow paths associated with the genesis and evolution of dolines must be clarified, thus collapse and bowl-shaped dolines should be hydrologically monitored. Copyright © 2016 John Wiley & Sons, Ltd.

KEYWORDS: dolines; peridotites; LiDAR; New Caledonia; fracture control

Introduction

Dolines – also termed sinkholes – are closed depressions and widespread features of karstic system landscapes (Ford and Williams, 2007). Several mechanisms have been proposed for their formation, which are described in Waltham and Fookes (2003). All the mechanisms require voids, either generated by dissolution of the host rocks focused by the doline itself or by growth and upward propagation of pre-existing voids. As voids can be observed in a variety of geological protoliths, dolines alone cannot be considered as proof of an underlying active

karstic system. Collapse dolines result from sudden collapse of hardened roof above existing voids (Gabrovsek and Stepisnik, 2011); suffosion dolines result from the entrainment of fine-grained non-cohesive material in the underlying karstic network. Dolines present a threat to surface infrastructures such as roads, houses and industrial areas (Mendonça *et al.*, 1994). Therefore several studies are dedicated to the statistical analysis of doline distribution in karstic areas (Milanovic, 2004; Basso *et al.*, 2013).

Morphometric analysis of dolines is commonly used as a quantitative tool in karst environment analysis and enables

the generation of hypotheses on the evolution and dynamics of karstic systems (Jennings, 1975; Day, 1983; Bondesan *et al.*, 1992). Further studies are encouraged by new and precise digital terrain models (DTMs) (Lyew-Ayee *et al.*, 2006; Telbisz *et al.*, 2009; Pardo-Iguzquiza *et al.*, 2013), which are now increasingly available thanks to light detection and ranging (LiDAR) technology (Shan and Toth, 2008; Vosselman and Maas, 2010; Höfle *et al.*, 2013; Siart *et al.*, 2013). According to McIlroy de la Rosa (2012), the use of the fast and sub-millimeter accurate LiDAR system with associated geographic information system (GIS) analysis allows an evolution from field data collection and personal interpretation to morphometric techniques in karst studies: this is our objective in this study, using a LiDAR DTM on the Massif du Sud, which is well known in New Caledonia for its numerous doline-type lakes.

Spatial analyses of dolines can provide new insights into their formation mechanism as illustrated by the pioneering work of Kemmerly (1976). A wide range of literature on their relationships with faulting (Gao *et al.*, 2005; Closson and Karaki, 2009) is available and numerical detection of the alignment of point-like features can be used (Lutz, 1986; Le Corvec *et al.*, 2013). Doline occurrence is linked to morphologic features of the drainage pattern (Segura *et al.*, 2007). Their mutual influence, as reflected by clustering, is usually assessed with nearest neighbor analyses (Clark and Evans, 1954; Kemmerly, 1982). Some of these well-known tools will be applied to the original context of ultramafic rocks.

The specificity of dolines in New Caledonia (Southwest Pacific) lies in their development on ultramafic protoliths, the Peridotite Nappe (Avias, 1967) obducted onto the New Caledonia basement

during the Late Eocene (Cluzel *et al.*, 2001; Cluzel *et al.*, 2012b). New Caledonia presents an exceptional surface of peridotites cropping out on nearly one third of Grande Terre, especially in the south (Figure 1a). Peridotites present extensive evidence for chemical weathering (lapiaz, dolines) but no extensive underground drainage system is recognized (Trescases, 1975; Genna *et al.*, 2005a, 2005b). Whereas limestone rocks are subject to almost 100% dissolution, weathering of ultramafic rocks leaves an insoluble *in situ* residue (Fritsch, 2012) that is able to clog voids generated by dissolution. Therefore, in New Caledonia, dissolution features on ultrabasic rocks are termed pseudokarstic. The weathering profile hosts economic concentrations of nickel (Ni) and cobalt (Co). Hence dolines are of general concern in mining operations, since these localized heterogeneities may impact both the consistency of Ni ore deposits and underground drainage systems.

After a presentation of the geology of the study area and of weathering of peridotites in a tropical climate, the method used to build a dataset of 8601 dolines is described. Then, a quantitative analysis of doline shape and spatial distribution is presented. Finally, a typology of dolines based on their morphological parameters is proposed and possible mechanisms governing their formation and evolution are discussed.

Geology and geomorphology of the study area

From a structural point of view, fracturing and related serpentinization of the Peridotite Nappe span a long period (c. 100 Ma) and correspond to general low temperature

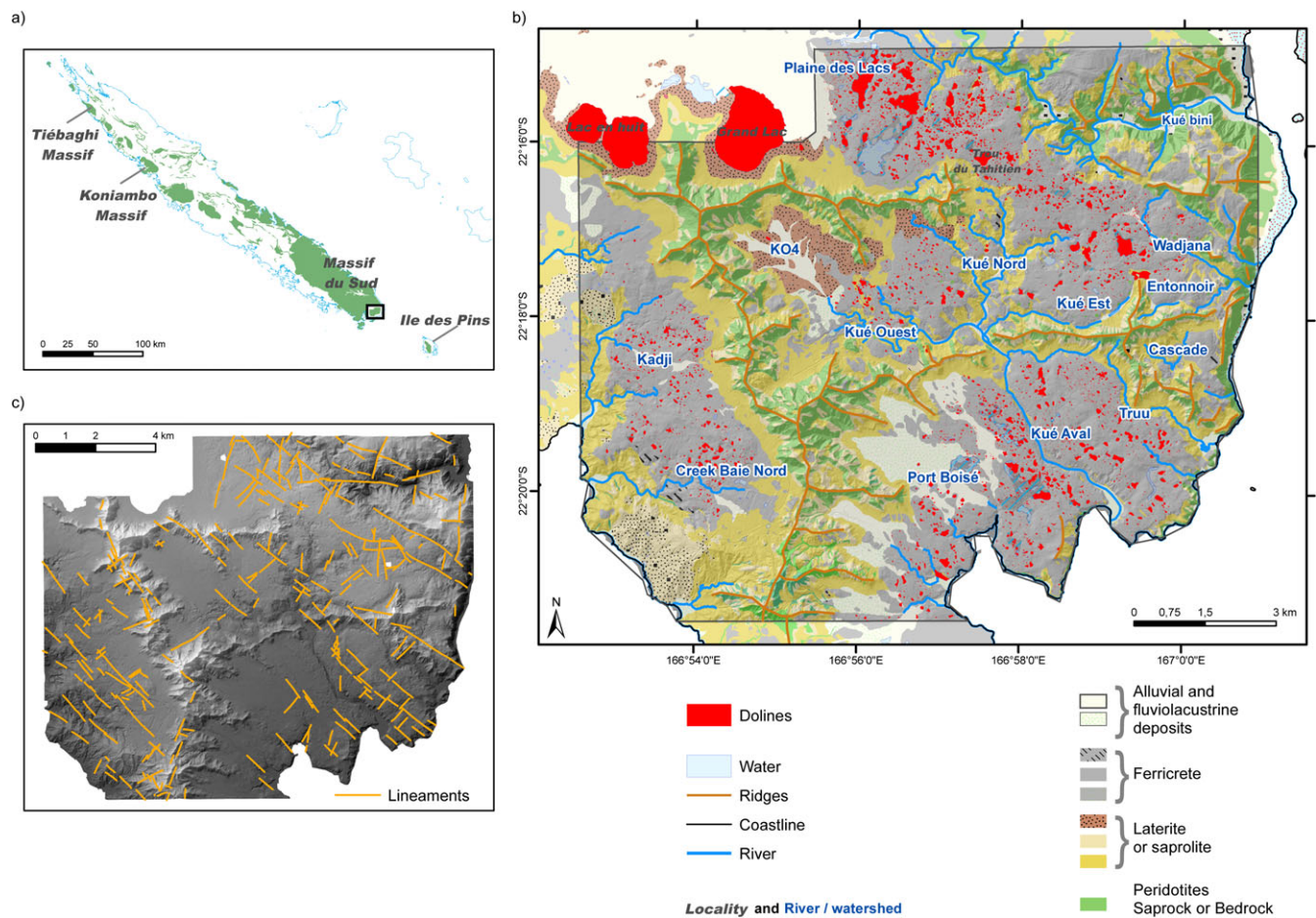


Figure 1. (a) General map of the Grande Terre island of New Caledonia with ultramafic formations mapped in green; (b) doline and main geological (Sevin *et al.*, 2012a), morphological and hydrological features mapped on part of the Massif du Sud. The area considered in this study is shaded; (c) geological lineaments of the study area superposed on the LiDAR DTM map.

hydration and cooling of the mantle protolith. The following geodynamic events are involved in the fracturing of the Peridotite Nappe: (i) Late Cretaceous oceanic seafloor spreading of the South Loyalty Basin (SLB) (Cluzel *et al.*, 2001); (ii) Palaeocene-Early Eocene convergence and subsequent Eocene subduction (Cluzel *et al.*, 2006; Maurizot, 2011, 2013; Maurizot and Cluzel, 2014); (iii) high-pressure/low-temperature exhumation of the Norfolk Ridge and obduction of the SLB oceanic lithosphere over the Norfolk Ridge during the Late Eocene (Cluzel *et al.*, 2001; Baldwin *et al.*, 2007); (iv) post-obduction unroofing of the obducted ultramafic terrane related to isostatic re-equilibrium (Lagabrielle *et al.*, 2005; Sevin *et al.*, 2014); (v) arrival of the New Caledonia block in Vanuatu's east-dipping active subduction zone and its forebulge (Dubois *et al.*, 1974).

Unravelling this complex succession of deformations is still an ongoing challenge. However, there is general agreement that major fracture directions observed in the Peridotite Nappe are N 130°–N 150° (Leguéré, 1976; Moutte and Paris, 1976), which also corresponds to the main elongation direction of Grande Terre. According to the same authors, subordinate conjugated N 90°, N 45° and N 0° directions are also locally observed. To explain these fracture directions, the following events may be identified: (1) the Late Cretaceous seafloor spreading period resulted in high temperature foliation, associated with dunite/harzburgite layering, and stretching lineation corresponding to asthenospheric flow. A north–south-oriented, kilometer-scale shear zone with vertical foliation is interpreted as a paleo-transform fault (Prinzhofer *et al.*, 1980; Titus *et al.*, 2011); (2) the Peridotite Nappe is cross-cut at all levels by a pervasive dyke system of dolerite, micro-diorite and felsic gabbros emplaced within a narrow span of time, (55–50 Ma or Early Eocene, Cluzel *et al.*, 2006) which, together with amphibolite lenses dated at 56 Ma in the basal serpentinite sole, are interpreted as evidence of the initiation of a subduction at the spreading ridge of the SLB (Ulrich *et al.*, 2010; Cluzel *et al.*, 2012a). These dyke networks are associated with the main N 130° and N 45° fracture fields (Maurizot, 2013); (3) Late Eocene obduction is marked by the development of porphyroclastic mylonitic serpentinite, 10 to 200 m thick, at the base of the Peridotite Nappe; (4) subsequent post-obduction deformation episodes occur at higher structural levels and in extensional regimes. Consequently, directions of fractures are scattered, although inherited structures are still dominant. In the north of New Caledonia, on the Tiébaghi massif (Figure 1a), the ultramafic protolith is covered by an extensive ferricrete with elongated dolines aligned along a dominant N 130° and a subordinate N 0° direction which corresponds to a fracture field associated with felsic dykes and developed in successive dextral, transtensional, and extensional regimes (Robineau and Join, 2005; Robineau *et al.*, 2007). A similar pattern is to be found in the Massif du Sud (Figure 1c); (5) late post-obduction evolution is characterized by limited vertical motions and eustatic variations (Folcher *et al.*, 2015). The forebulge resulting from the eastward dipping subduction of Vanuatu affects the Loyalty Islands (Dubois *et al.*, 1974; Bogdanov *et al.*, 2011) and likely the southeast coast of the Massif du Sud and Ile des Pins, where the 125-ka-old fringing reef is uplifted by c. 10 m (Cabioch *et al.*, 1996). In the study area, these late-stage events resulted in a tilt of the ferricrete surfaces which are uplifted to the north and lowered southward.

From a lithological and geochemical point of view, the Massif du Sud protolith is mostly formed by upper mantle rocks (i.e. harzburgite, dunite). Olivine and orthopyroxene, the main constitutive silicates, are reactive and soluble minerals in a humid tropical climate (Thomas, 1994). Pervasive weathering removes elements such as magnesium (Mg), calcium (Ca) and

silicon (Si), and leaves *in situ* less soluble elements such as aluminum (Al), iron (Fe), manganese (Mn), nickel (Ni), and cobalt (Co), with the latter two forming economic deposits. As a consequence of this subtractive process, the remaining laterite profile is mainly constituted of Fe oxi-hydroxides. A complete differentiated profile comprises, from base to top (Figure 2), saprock (20% of weathered rock), saprolite, where inherited bedrock textures are still recognized but mass loss is significant, laterite where all initial textures are removed, and ferricrete on top. Thickness of the profile may reach 40 m to 80 m (Freyssinet *et al.*, 2005; Sevin, 2014). However, weathering is a complex process that includes chemical reactions such as leaching and precipitation of matter, but also mechanical processes such as compaction, collapse, and underground water transport of particles either in solution or in suspension. It is currently admitted that complete chemical weathering of ultramafic rocks is associated with volume reduction as 1 m of laterite results from the weathering of 6 m to 9 m of unaltered peridotites (Fritsch, 2012; Fritsch *et al.*, 2014).

Thorne *et al.* (2012) specify that climate is a major control on Ni laterite formation. Areas currently conducive to Ni formation receive more than 1000 mm/yr precipitation, have a cold month mean (CMM) temperature of between 15 °C and 27 °C and a warm month mean (WMM) temperature of between 22 °C and 31 °C. Current meteorological conditions in the study area involve between 2200 and 3100 mm annual rainfall and a 22 °C mean temperature (19.2 °C for CMM and 25.9 °C for WMM), according to Météo France (2007), which is consistent with tropical weathering. According to Sevin (2014), in comparison with Australia, the New Caledonian climate is moderate to warm and humid from Oligocene to Miocene, warm humid to semi-arid during Miocene, and probably arid/semi-arid to humid during Pliocene. Therefore, combined with eustatic variations, New Caledonia recorded several superimposed phases of weathering (Chevillotte *et al.*, 2006; Sevin *et al.*, 2012b).

The hydrogeological model of weathered peridotites (Figure 2) is a multilayered model (Join *et al.*, 2005) with, from top to bottom: (i) a temporary perched aquifer on ferricrete; this layer favors infiltration and temporary springs flow from its bottom; (ii) an aquitard on semi-pervious laterite and saprolite; (iii) the principal aquifer included in saprock and upper fractured peridotites; (iv) bedrock. Underground circulation can take place in the fresh peridotites through deeper fractures.

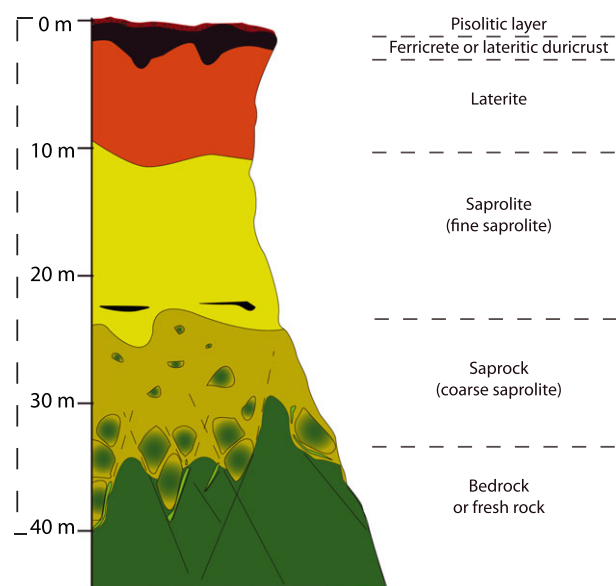


Figure 2. Weathering profile of New Caledonia peridotites.

Pseudokarst network is assumed to develop in the saprock aquifer since hydraulic conductivities larger than 10^{-4} m/s are recorded in this layer (Jeanpert, 2010). Thickness of the principal aquifer including saprock and fractured peridotites is an ongoing research topic. In Oman, where weathering processes are very weak due to the arid climate (absence of ferricrete, laterite and saprolite), the thickness of the fractured peridotites has been estimated at around 50 m (Dewandel *et al.*, 2005). In New Caledonia, according to initial results from borehole data on the Koniambo Massif (see Figure 1a), fractures can occur down to a depth of 200 m (Jeanpert and Dewandel, 2013).

From a geomorphological viewpoint, weathering leads to flattened landscapes. The downward progression of the weathering front tends to isolate individual cells or basins covered by thick soft laterite, capped by resistant ferricrete, and surrounded by residual unweathered peridotite ridges (Trescases, 1975). On the west coast of Grande Terre, erosion has isolated klippe of peridotites (Figure 1a) which are highly incised and surface drained. In the Massif du Sud, initial morphology such as basins and cells surrounded by peridotitic bedrock is preserved. Sinks, springs and endorheic watersheds are observed. Tracer tests revealed pseudokarstic behavior on some parts of the study area (Entonnoir and Cascade watersheds, see Figure 1b). Two domains are delimited by a complex set of faults (Folcher *et al.*, 2015); to the northeast the ferricrete basins are uplifted and incised by active river systems while to the south and west continuous smooth landscapes are exposed and fluviolacustrine deposits are observed (Figure 1b). Dolines constitute the main, and nearly the only, surface expressions of pseudokarst; consequently their spatial distribution and characterization may give important information on groundwater systems and Ni ore distribution.

Materials and Methods

Materials

Vale NC, a subsidiary of the major mining company Vale, operates a world-class nickel-cobalt deposit in the south of the Massif du Sud (Goro plateau open pit and related infrastructures). LiDAR data were acquired by Vale NC on a commercial basis through an airborne survey at 600 m altitude along east-west (E-W) lines between October 26 and November 2, 2006, i.e. during the slightly cloudy season. The airborne operation was associated with a ground global positioning system (GPS) field survey. The position of the aircraft was recovered using an inertial unit and continuous GPS recording. Elevation data were subsequently classified into ground and non-ground points using a single software and cross-checking the elevation values and the reflected intensity of the laser beam. The laser scanning frequency was in the order of 50 000 Hz and the average footprint of the laser beam was 25 cm. Data were delivered to Vale NC both as a raw file including nearly 95 000 000 data points and as an interpolated $1\text{ m} \times 1\text{ m}$ DTM. This DTM, provided by Vale NC for the purpose of this study,

covers an area of around 148 km^2 . Elevation ranges from 0 m to 587 m. The vertical accuracy of the DTM was assessed by the company against ground GPS data and the resulting standard error was 3.3 cm RMS (root mean square).

Geomorphological and geological data are extracted from the Geological Survey of New Caledonia (SGNC) database at a 1:50 000 scale. Major lineaments are defined by orthophoto-interpretation, from scarps as well as doline elongations and alignments. Topographic features like coastline, rivers and ridges are extracted from the Direction of Topography and Terrestrial Transport (Government of New Caledonia) topographic database at a 1:10 000 scale.

Annual rainfall is provided by Météo France as a $1\text{ km} \times 1\text{ km}$ grid computed from regression as a function of topography of 120 rain gauges in New Caledonia (Benichou and Le Breton, 1987). The method (AURELHY model) uses 10 eigenvectors computed by principal component analysis (PCA) over New Caledonia (Leou Tham, 2005); the first eigenvector characterizes the positive correlation between rainfall and altitude, while other vectors refer to topographic features influencing rainfall, such as exposure to trade winds.

Methodology used for doline mapping

Dolines are mapped using the ArcGis 10.2@ software by filling depressions up to the water overflow level, according to the method discussed in Telbisz *et al.* (2009) and Pardo-Iguzquiza *et al.* (2013). Since the majority of large dolines were flooded at the time of the LiDAR survey and as LiDAR is reflected by the water surface, individual sinkholes within these dolines were not detected. Fieldwork during the dry season revealed that smaller sinkholes did exist in some of the large dolines. This prevents the definition of a rank for each sinkhole according to the method set out in Obu and Podobnikar (2013) and Kobal *et al.* (2015).

Mapping results from several calculation steps are summarized in Figure 3. Of particular note is that although steps 1, 2 and 3 can be completely automated, step 4 requires processing to remove some depressions manually. This involves validation from aerial photography to eliminate artifacts like roads, tracks, pits due to mining activity, and unrealistic objects like LiDAR artifacts.

Definition of morphometric parameters and correlation analysis

Morphometric analysis presented in this paper is built on previous limestone doline analysis (Sustersic, 1994) and uses parameters described later.

Automatic calculations and mapping involve approximations on the values of real doline parameters (surface, depth or slope for example). Nevertheless, since the same methodology is applied on all 8601 dolines, comparison between their morphological parameters is consistent. The following parameters are

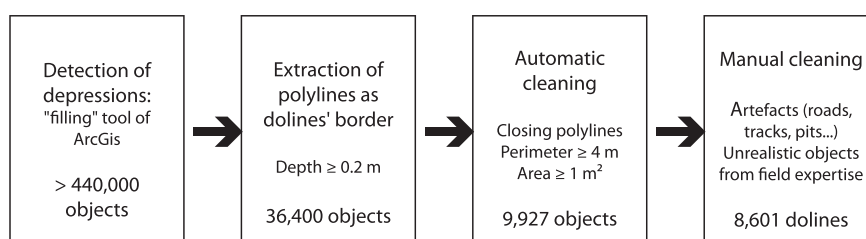


Figure 3. Flow chart of the methodology used in doline detection and mapping.

computed: the area (A), perimeter (P), lengths of the longest and shortest axis. Depth and volume of the dolines are computed from the results of the filling tool of ArcGis® 10.2. It should be noted that since the laser beam of the LiDAR is reflected on water surfaces, the volume and depth of ponded dolines are underestimated. The equivalent radius R_{eq} is calculated considering the radius of the circle which has an area equal to the doline's area. The Gravelius coefficient

$$C_g = \frac{P}{2 \cdot \sqrt{\pi \cdot A}}$$

is estimated, and characterizes the compactness of the doline outline. It is equal to one for a circular doline and larger than one otherwise. The local slope is computed for each cell of the DTM. Mean slope is then extracted for each doline. The distance between the centroid of the doline and its deepest point is considered as an indication of the gap between its shape and a perfect conical shape. The direction of the major axis of each doline is extracted, and the direction of the vector from centroid to deepest point is also calculated.

These parameters are referred to as morphometric parameters in contrast with environmental parameters such as rainfall or distance to the nearest river. The dataset of morphometric parameters is analyzed using PCA: it includes the 11 individual parameters of each doline: length, width, perimeter, area, mean slope, depth, volume, equivalent radius, Gravelius coefficient, distance between the centroid and the deepest point of the doline, and lastly, the direction of the major axis.

Fieldwork

Extensive fieldwork is associated with the computational analysis of the LiDAR DTM. In particular, special attention is given to features bounding dolines, the shape of dolines, and the smallest dolines, as it is generally considered that dolines should have diameters larger than 10 m (Kobal *et al.*, 2015) whilst the LiDAR DTM allowed the detection of sinkholes down to 1 m². Moreover, fault analysis is carried out where outcrops are available to complete and validate remote sensing lineament detection.

Methods used for spatial distribution analysis

Spatial distribution of dolines is firstly analyzed through doline density models obtained at various length scales by computing for each point of a regular mesh grid the convolution of the doline centroid distribution with a normalized Gaussian kernel (Wand and Jones, 1995):

$$\rho(x_0, y_0) = \frac{1}{\pi L^2} \sum_{i=1}^{Ndol} \exp\left(-\frac{(x_0 - x_i)^2 + (y_0 - y_i)^2}{L^2}\right) \quad (1)$$

where L is the length scale of the density model, $\rho(x_0, y_0)$ the doline density at point (x_0, y_0) , and (x_i, y_i) the coordinates of doline i , while N_{dol} is the total number of dolines, i.e. 8601.

Spatial distribution of the dolines is also analyzed by a PCA applied to an environmental parameter dataset including distance to characteristic morphologic features such as ridges and rivers. Only the perennial river sections are considered in the spatial analysis. Faults are not considered here since geologists use doline alignments to infer and draw faults in this area, which can lead to spurious results. Annual rainfall, doline density, and elevation are linearly interpolated at the doline

position. Strictly speaking, the doline density at a doline point is infinite, therefore a smooth density is interpolated from the $L=250$ m density model, after checking that the correlation results are not strongly sensitive to the length scale L of the density model. Moreover, as no hydraulic head map is currently available for the region, smoothed topography deduced from LiDAR data is used as a proxy for hydraulic heads, which are known to closely follow topography in basement aquifers. Estimation of the hydraulic gradient is calculated from the slope of the smoothed LiDAR grid on a 500 m resolution grid, in order to represent the regional hydraulic gradient. Moreover, the topographic slope is calculated on a 50 m resolution grid as a local slope, representative of the doline's geomorphologic environment.

Then, size distribution of dolines is compared to distribution of lakes in either flat or mountainous areas. Shorelines are known to present fractal geometries (Mandelbrot, 1983). Matsushita *et al.* (1991) have shown that this resulted in a power law distribution of lake sizes, which corresponds to a linear trend on a log-abundance log-size plot, and that the slope of the regression line is equal to minus half of the fractal dimension of the shorelines. In the case of mountainous areas, where lakes are far from mean altitude, Seekell *et al.* (2013) show that their size distribution deviates from a power law distribution, but can be approximated by a more general law of the form:

$$N = c \times A^{-b} \times e^{-dA} \quad (2)$$

where N is the abundance, A the area, and b , c and d are fitting parameters with b equal to half of the fractal dimension of shorelines as in the power law distribution. The second term introduces a faster decrease of N with increasing areas, which can be interpreted as the effect of the lack of sufficiently flat areas to produce large lakes in mountainous zones. Seekell *et al.* (2013), using a dataset of 1469 lakes with areas in the range of $[10^{-3}; 2]$ km², show that in the Adirondack Mountains the power law relationship does not apply but that Equation 2 is valid. Up to now, Equation 2 has not been checked in any karstic or pseudokarstic areas such as the Massif du Sud in New Caledonia. Moreover, the accuracy of LiDAR data will allow the checking of extension of Equation 2 to metric-sized features.

Lastly, as fractures are known to control early stages of karst development in limestones (Ford and Williams, 2007), the relationship between dolines and fractures is carefully explored. However as doline alignments are used to define fractures, an analysis independent of known fractures is required. Two methods are compared: the two-point alignment method based on the azimuth distribution of straight lines joining two dolines chosen randomly (Lutz, 1986), and a second method, developed for the study, in which alignment statistics are deduced from the number of aligned dolines along kilometeric length strips of various orientations.

Results

Doline dataset and morphological analysis

General mapping

The spatial distribution of dolines, extracted from LiDAR DTM data, is represented in Figure 1b. Automatic mapping identified 36 400 dolines; further processes, including manual cleaning (Figure 3), allowed the final dataset to be refined down to 8601 dolines. The map (Figure 1b) firstly reveals that dolines

are mostly clustered and almost exclusively on ferricrete. In addition, dolines are unevenly distributed among the different watersheds of the study area.

Morphometric parameters: overall characteristics

Frequency distributions of morphometric parameters are presented in Figure 4. These data show that the depressions are dominantly small: 80% of them have a R_{eq} smaller than 8 m, and 15% are smaller than 4 m², 35% less than 10 m² and

70% less than 100 m². Depression depths are lower than 4 m for 97% of them, and lower than 1 m for 80%. One single object, known as the Trou du Tahitien, is deeper than 25 m. 83% of the slopes are lower than 10°. More than 60% of dolines are nearly circular and characterized by a Gravelius coefficient equal or smaller than 1.1. The direction of the major axis (doline elongation) of the dolines is characterized by one maximum at around N 140°, although the direction of the shift of doline centers is maximum at around N 160°–170°.

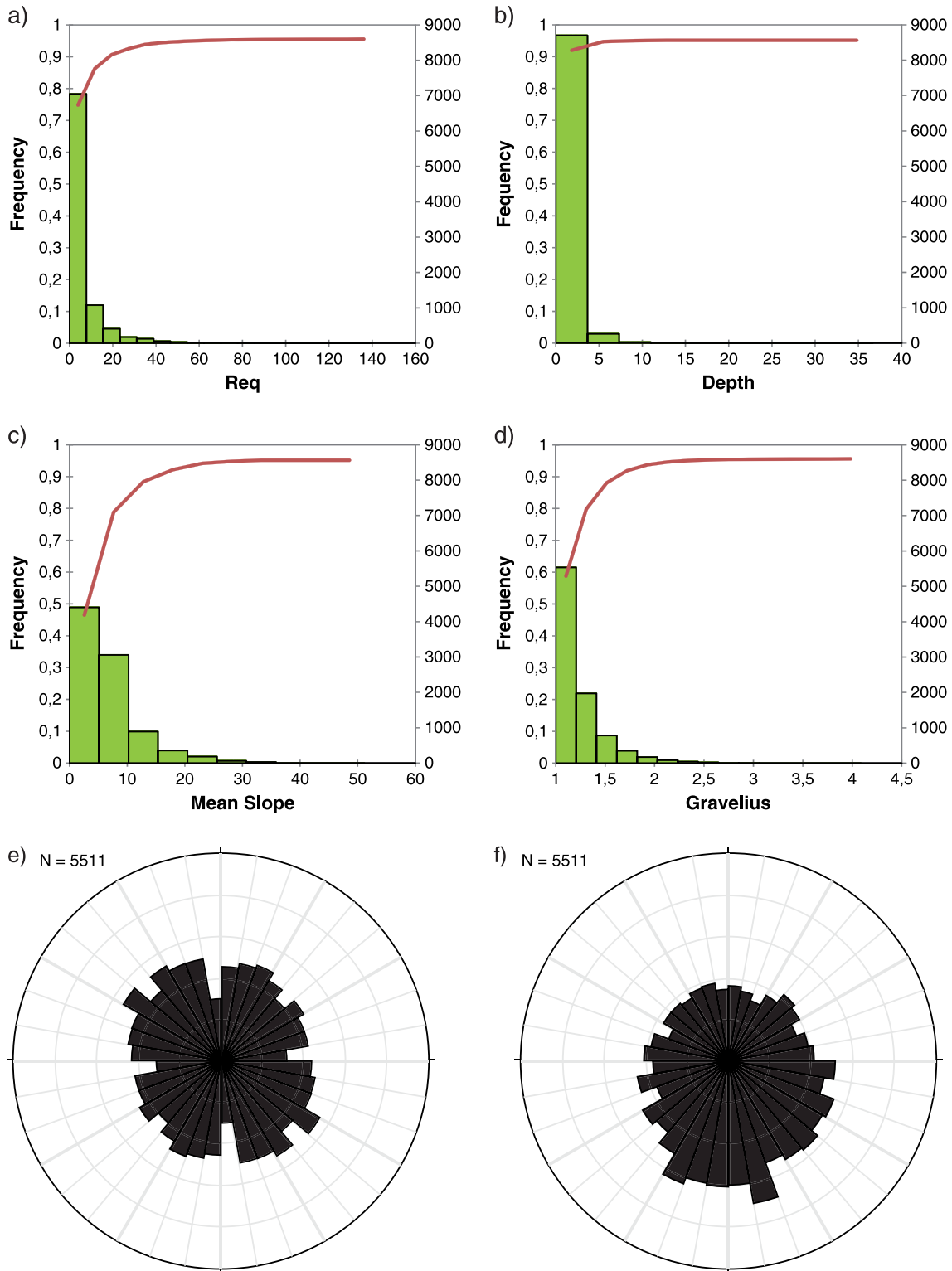


Figure 4. (a)–(d) Morphometric parameter distributions represented as graph frequency histogram and cumulative number of doline curves. (a) Equivalent radii (in meters). The largest dolines corresponding to $R_{eq} > 180$ m are not included; (b), (c) and (d) refer to the maximum depth (in meters), mean slope (°), Gravelius coefficient (compactness) C_g ; (e) is the direction of the major axis of the 5511 dolines larger than 10 m²; (f) is the direction of the vector joining the centroid to the deepest point for the 5511 dolines larger than 10 m².

Doline spatial distribution analysis

Density models

Doline density models obtained for various length scales L are displayed in Figure 5. For a length scale $L = 50$ m (Figure 5a) doline density is visually similar to their actual distribution. With an increasing scale, dolines appear to be organized as a series of high-density bands oriented between $N 120^\circ$ and $N 160^\circ$ (Figure 5b). When L continues to increase above 500 m, these bands are smoothed (Figure 5c) and two high concentration zones of dolines occur at the northern and south-eastern part of the modeled area. Maximum density increases with decreasing L . When L continues to increase beyond 1000 m, modeled doline density tends to reach the total number of dolines over the entire modeled area, i.e. 58.1 doline/ km^2 . A common feature of all these maps is that high-density areas are located in the main north and southeast watersheds, in the Plaine des Lacs and Kué Aval (see locations on Figure 1b). Density maps (not shown here) built for the smallest dolines ($1 \text{ m}^2 < \text{area} < 4 \text{ m}^2$ or $4 \text{ m}^2 < \text{area} < 10 \text{ m}^2$), are very similar to those of the entire dataset when normalized to the total number of considered dolines. These doline density maps clearly show high heterogeneity in doline distribution which could lead to strong anisotropy in an azimuth distribution analysis.

Principal component analysis (PCA)

A correlation matrix and a PCA are calculated for two datasets: the former describes the shape and size of dolines (morphometric parameters, Figure 6a), whereas the latter describes the doline environment (Figure 6c). Axes with a weight greater than 10% are considered as representative (Figures 6b and 6d). As expected, morphometric parameters of individual dolines, i.e. length, width, perimeter, area, equivalent radius and distance between the centroid and deepest point, are highly correlated (Figure 6a). The Gravelius coefficient presents some slightly positive correlation with the doline size (i.e. larger dolines have complex outlines) and a slightly negative correlation with slope (i.e. circular dolines tend to be small and steep). As expected too, mean slope and depth are correlated but no correlation is observed with size parameters. However, the direction of the major axis is not correlated with any other shape parameter and represents the third axis of the PCA with a weight equal to 9.2%.

Similar calculations on environmental parameters indicate that altitude and rainfall are strongly correlated (Figure 6c). Doline density is slightly correlated with these two parameters

and with the distance to rivers and ridges also. Local slope and regional hydraulic gradient present a slightly negative correlation with doline density. The first two axes are held by altitude, rainfall, slopes, density and distance to rivers (Figure 6d). Distance to ridges is not well correlated to any other environmental parameters and represents the third axis of the PCA with a weight equal to 14.0%. Dolines are located on flat areas (where the weathering profile is preserved) rather than on ridges where mechanical erosion prevails or in the vicinity of rivers where headward erosion occurs. The present hydraulic gradient does not have any control on doline distribution while altitude, rainfall and distance to rivers explain 34% of the data variance. The other correlations provided in Figure 6c relate to the morphology of the watersheds: local slope decreases when the distance to rivers increases, especially on the largest watersheds located in the northern area (i.e. the Plaine des Lacs region).

Size versus frequency analysis

The log abundance – log size plot of the entire dataset (Figure 7) does not fit a single straight line (power law relationship) or Equation 2. However, Figure 7 shows two different trends: (i) dolines that are smaller than $20\,000 \text{ m}^2$ can be closely fitted by Equation 2 with $[b; c; d] = [0.5; 2.0 \times 10^4; 1.0 \times 10^{-4}]$. Since b is half of the fractal dimension of the shorelines of dolines, this implies that their dimension is one and these shorelines are therefore not fractal. This is due to the fact that most dolines are nearly circular or ellipsoidal in shape; (ii) dolines that are larger than $20\,000 \text{ m}^2$ are significantly shifted compared to the previous curve, and can be fitted by a straight line with a 0.8 slope corresponding to a 1.6 fractal dimension of shorelines. This is consistent with the observation that larger dolines are non-circular and probably result from coalescence of several individual dolines. However, this last result should be considered carefully since the regression only relies on six points of the plot, which corresponds to a cumulated number of 30 dolines, and only two dolines larger than $250\,000 \text{ m}^2$. In contrast, no rupture in the log abundance – log size plot for smallest dolines is observed.

Alignment analysis

Doline density models of Figure 5 define kilometeric-long bands of dolines along a $N 130^\circ$ – $N 140^\circ$ direction, which is the main known fracture direction observed in the Peridotite Nappe in New Caledonia (Cluzel *et al.*, 2001). These bands are visible on the $L = 50$ m and $L = 250$ m models and are smoothed on the $L = 1000$ m model. This observation is mathematically verified later and resulting directions are compared with

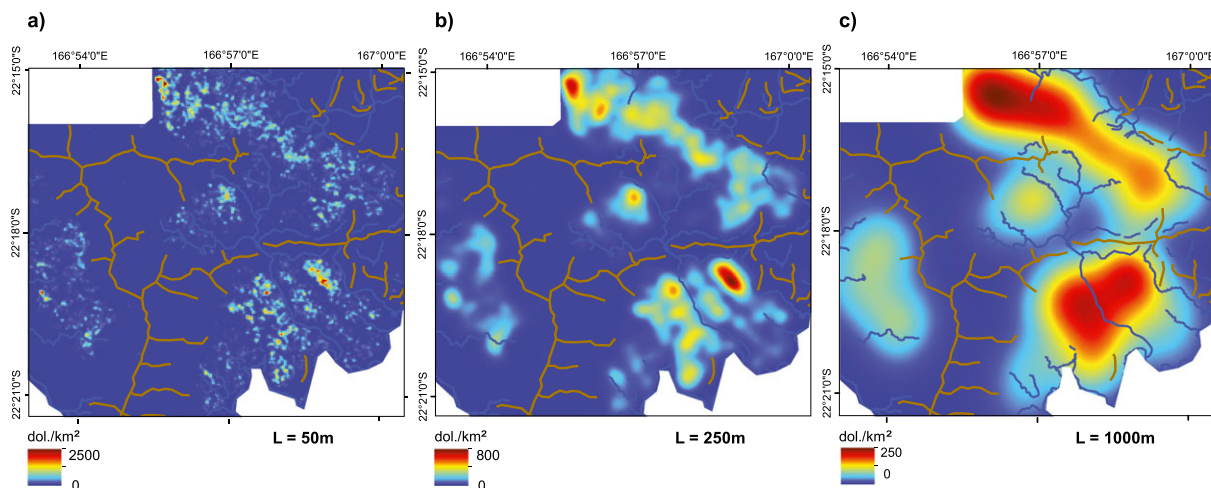


Figure 5. Doline density estimates computed by convolution with a Gaussian kernel of radius L : (a) $L = 50$ m, (b) $L = 250$ m, (c) $L = 1000$ m. Major topographic features are represented (ridges and rivers).

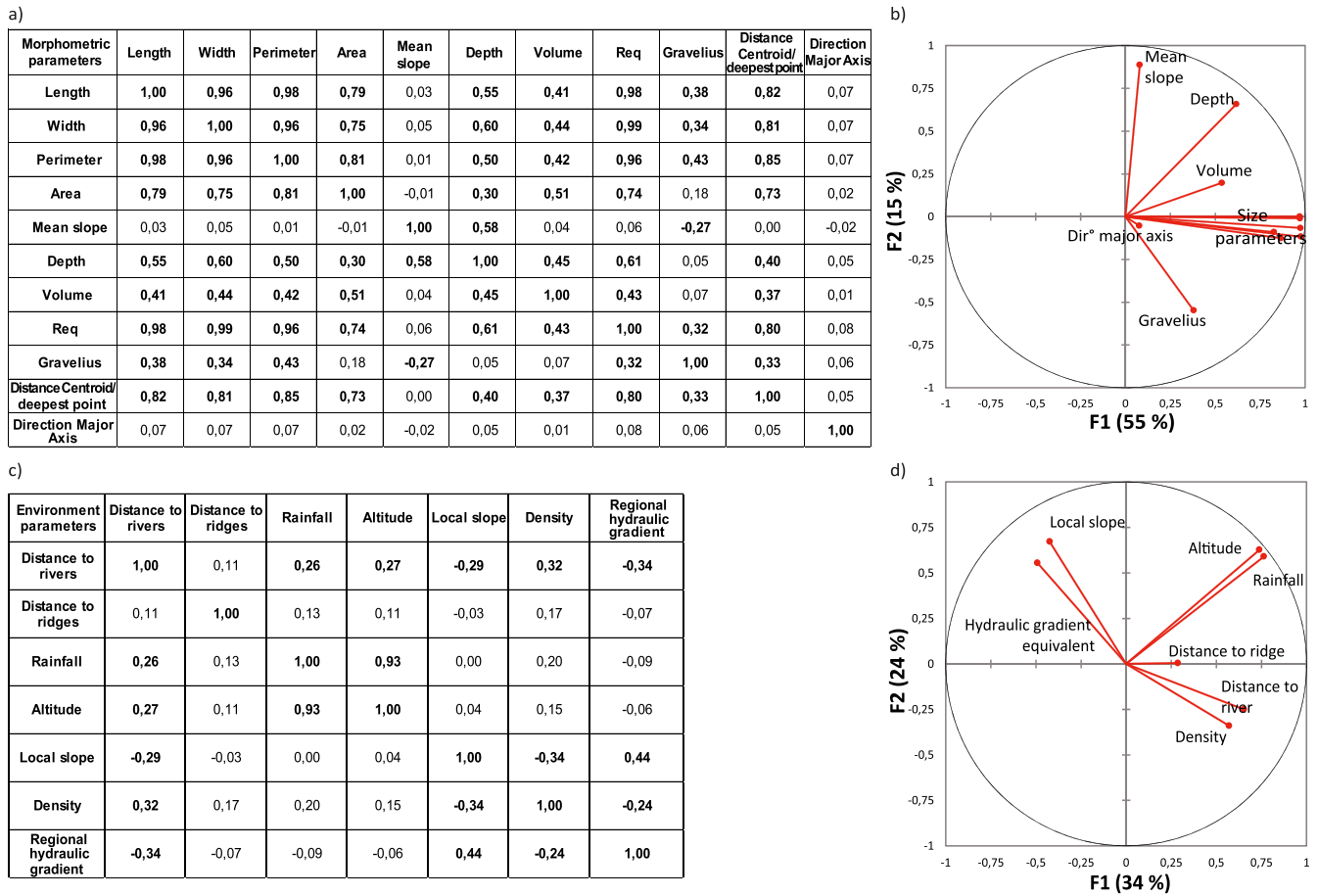


Figure 6. Principal component analysis (PCA) results: correlation matrix and projection of the main variables on the F1–F2 planes, F1, F2 being the principal components with decreasing explained variances; (a) and (b) refer to morphometric parameters, size parameters on (b) refer to R_{eq} , width, area, perimeter, length and distance from centroid to deepest point; (c) and (d) refer to environmental parameters.

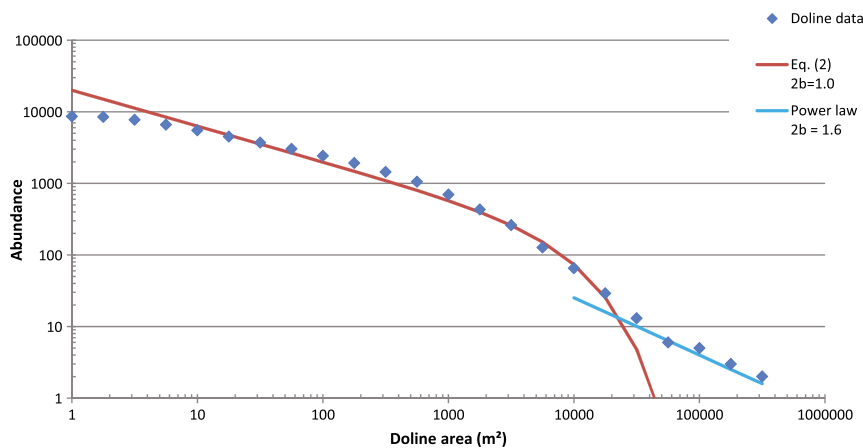


Figure 7. Cumulated number of dolines as a function of their area. The distribution can be fitted by Equation 2 for dolines between 4 m² and 20 000 m² and by a straight line above.

lineament detection from remote sensing and additional fracture outcrop measurements.

Fracture orientation from remote sensing and field data

Two datasets of lineaments defined by orthophoto-interpretation are extracted from the geological database of the SGNC: the first one corresponds to observations on bedrock whereas the second one refers to observations on the regolith (Figure 8). Overall there is good coherence between the two datasets, which shows that regolith lineaments reflect the deeper bedrock structuration.

The major N 130° structural direction appears on both lineaments and measured fractures on outcrops (Figures 8b–8d). A minor N 40°–50° direction is also observed on lineaments and measured fracture data (Figures 8b and 8c), while a N 0° is only observed on bedrock lineaments (Figure 8d).

Two-point azimuth distribution

Results of azimuth distribution of straight lines joining two dolines randomly chosen are displayed in Figure 9 for real data and for synthetic data randomly generated according to the

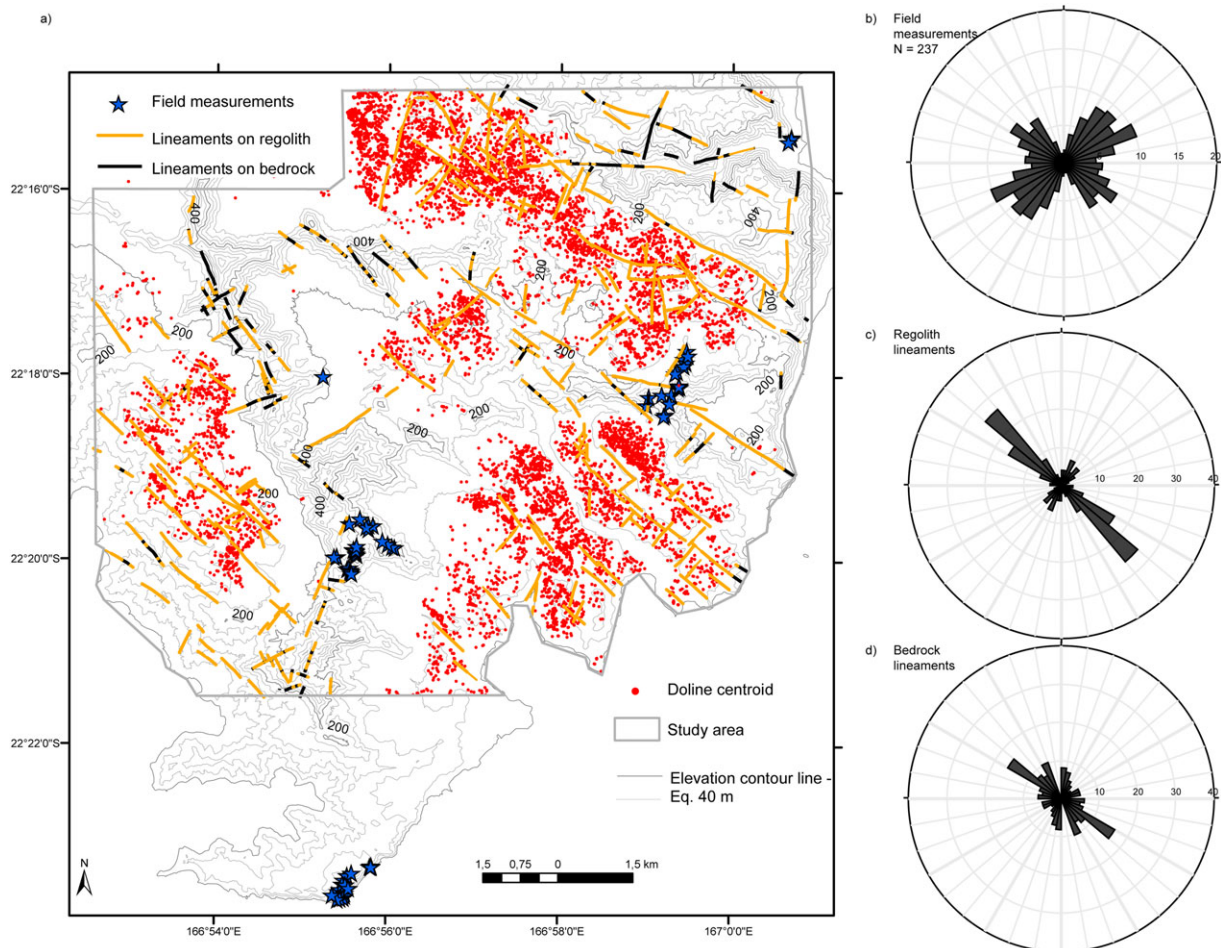


Figure 8. Fracture measurements: (a) map of field observation points and lineaments on 10 m resolution DTM map; (b), (c) and (d) are azimuth distribution of field measured fractures at outcrop, of lineaments on regolith and of lineaments on bedrock. Lineaments are weighted by their length.

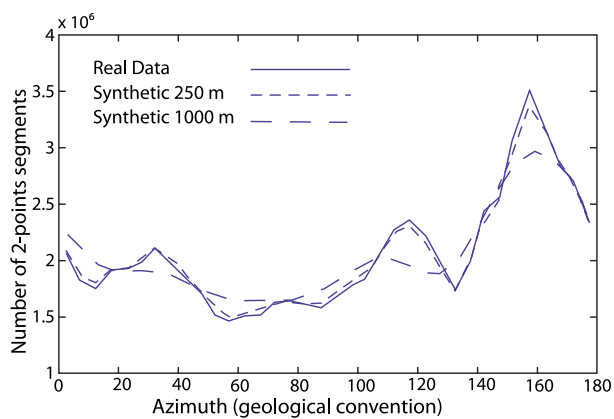


Figure 9. Two-point azimuth distribution for real dolines and for synthetic density models.

density models displayed in Figure 5. Since the real two-point azimuth distributions and those computed from randomly distributed synthetic data generated with density models up to a length scale of 250 m are almost identical, we conclude that the density distribution of dolines, rather than their exact location, is responsible for anisotropy in the two-point azimuth distribution. Distributions are characterized by a main peak at N 157.5°, and two minor peaks at N 32.5° and N 117.5°.

Doline alignment

Kilometer-scale alignments consisting of up to 20 dolines are observed by careful examination of the doline distribution map (Figure 1b). We therefore try to determine an alignment detection based on the features observed on real data. For each of the 8601 dolines, we compute the number of dolines included within a 1-km-long and 2 l-wide strip extending in a given direction and centered on the doline. The half-width l corresponds to the distance at which fractures control doline generation. As previously mentioned, this orientation distribution is compared with those obtained with synthetic doline distributions generated randomly according to the different density models of Figure 5. A value of $l = 10$ m is selected, as deduced from the visual alignment of real dolines and after having checked that increasing this value to $l = 25$ m does not affect the position of alignment peaks. The associated results are displayed in Figure 10. Similar results (not provided in this paper) are obtained when selecting the smallest dolines only. Alignment of real dolines is clearly different from those obtained with synthetic data. It presents a peak near N 140°, which corresponds roughly to the main fracture direction of Grande Terre. Yet some local N 50° alignments are visible on the map in Figure 1b. This direction is also observed on the field measurements and remote sensing data (Figure 8), but not enough dolines are involved to be detected in the statistical analysis, which only extracts the main N 140° direction. When introducing a smoothed doline distribution, even with a kernel of radius 50 m, this peak is smoothed, and the mean number of aligned doline decreases. With a smoothing length of 250 m, the

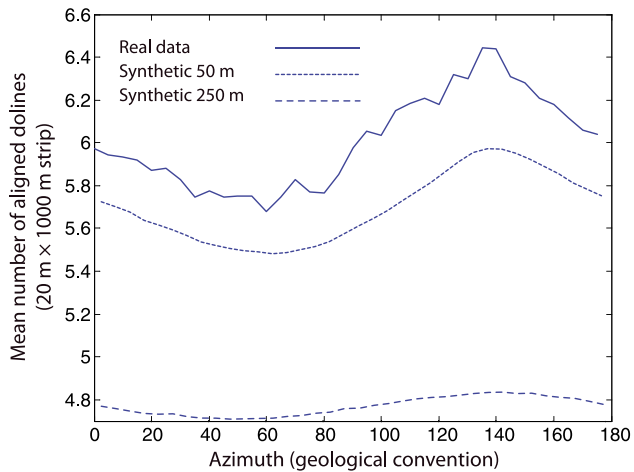


Figure 10. Doline alignment (number of dolines in a 1 km × 20 m strip) for real dolines and for synthetic density models.

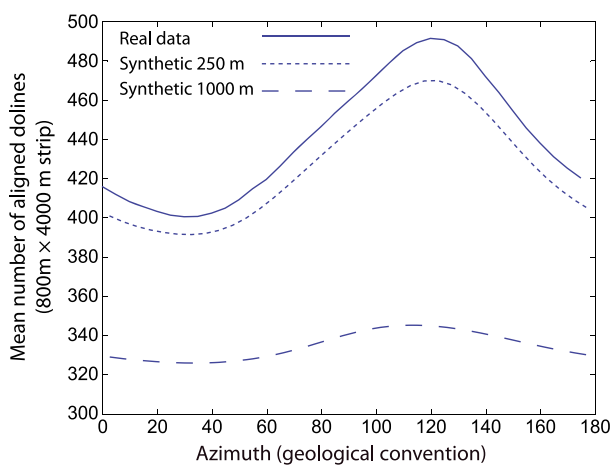


Figure 11. Same as Figure 10 for a 4 km × 800 m strip.

peak almost disappears, and the mean number of aligned dolines subsequently decreases to nearly 4.7. If doline distribution is smoothed further, curves continue to flatten and the mean number of aligned dolines decreases as well. The minimum number is obtained with a uniform doline distribution in the modeled area, i.e. 58.1 dolines/km². For this uniform distribution, the number of aligned dolines is given by the surface of a 1-km long and 20-m wide strip, i.e. nearly 1.16. Since the single peak near N 137.5° is reduced by smoothing the actual doline location with a 50-m wide Gaussian kernel, it is concluded that dolines are aligned with a tolerance of less than 50 m. Slightly different alignment statistics are obtained if larger strips are considered, for example with 4-km long strips and $l = 400$ m (Figure 11). This is interpreted as a consequence of the high-density doline bands observed on Figure 5.

Consequently, all these results evidence that dolines are concentrated on two watersheds. The alignment of these two watersheds is oriented N 157°. Within these watersheds, dolines are concentrated in high-density strips along a mean N 120° direction, whereas individual dolines defined alignments along a mean N 137.5° direction.

Discussion

Inclusion of the smallest topographic depressions detected by LiDAR in the doline dataset

Depressions smaller than the resolution of LiDAR data are considered as artifacts and are discarded. However, the dataset

still reveals a large number of small depressions (15% are smaller than 4 m² and 35% smaller than 10 m², see also Figure 4), while only depressions larger than 10 m in diameter are considered as dolines in limestone karst (Kobal *et al.*, 2015). Fieldwork confirmed that dolines larger than 4 m² are always identified as depressions limited by ferricrete blocks, indicating a collapse origin. Moreover, small dolines (surface <4 m² or 4 m² < surface <10 m²) present similar density and alignment statistics to the entire dataset. These results validate the choice made to include them in the doline dataset. Furthermore, they represent a potential hazard due to their possible evolution toward large dolines.

Doline abundance and density

Doline abundance as a function of their size presents two different trends below and above a threshold area of 20 000 m². Below this limit, doline abundance can be reasonably accounted for in the general equation proposed by Seekell *et al.* (2013) for lakes in mountainous areas, yet with a dimension of one. This dimension indicates that the shape of doline shorelines does not depend on the scale of observation, as opposed to lake and sea shores. This also highlights the observation that small dolines are slightly elongated objects, as evidenced by their moderate Gravelius coefficient. However, the 30 dolines larger or equal to 20 000 m² differ from this relation and are aligned along a 0.8 sloped regression line, corresponding to a fractal dimension of 1.6. Indeed, large dolines present more complex shapes and seem to result from the coalescence of several initially round-shaped dolines. This could be an indication that, as for lakes, the shorelines of these large dolines are controlled by mechanical erosion and sedimentation.

According to the PCA and field observations, doline density is strongly controlled by three parameters. The first one is the weathering state, dolines being observed only on ferricrete, and more precisely on flat areas where the entire weathering profile is preserved (Figure 1b). Thus, doline initiation seems to require the presence of ferricrete, which matches with the fact that the smallest dolines usually result from ferricrete collapse. The second parameter is altitude (or annual rainfall, since rainfall increases markedly with altitude). The highest doline densities are found on the north and southeast of our study area, in the Plaine des Lacs and Kué Aval watersheds, which correspond to uplifted areas. Considering that increasing altitude means increasing rainfall and decreasing temperature (i.e. less evaporation), one might conclude that doline density is partly governed by the amount of rain that infiltrates. Since the high porosity of ferricrete promotes infiltration, both the first and second parameters connect doline density to the weathering power of rain. The last parameter is the distance to topographic ridges. This can be understood by considering that ridges consist of outcropping rocks, and that mechanical erosion removes weathered material. The role of mechanical erosion is also consistent with the positive correlation between doline density and distance to rivers since development of a river network in a pre-existing doline network could result in dolines disappearing in the high slope area surrounding the river.

No clear relationships between doline density and hydraulic gradient (estimated from the regional topographic slope) have been found. On the Plaine des Lacs, the highest doline density is found at the north-western part of a northwest–southeast (NW–SE) trending watershed, 2 km away from the coast, while its central part presents nearly half of the maximum doline density, although it is located along the Kué Bini River, flowing inside a deeply incised valley down to below 100 m in altitude.

The present hydraulic gradient is thus not the most significant parameter in the doline density versus altitude relationship.

Relationship between dolines and fractures

There is a clear relationship between doline density and fractures, especially when considering the N 130°–140° major fracture direction of Grande Terre commonly observed in the field (Figure 8). This fracturing is inherited from the initial obduction of ophiolitic rocks, and repetitively re-activated during subsequent tectonic events (Moutte and Paris, 1976; Cluzel *et al.*, 2001). Two-point alignment statistics provided information on the general density distribution of dolines but not on the alignment of dolines themselves. However, a more efficient method, based on the number of dolines included in a 1 km × 20 m strip allows the detection of a single alignment peak along the N 137.5 ± 5° direction. The peak decreases if the doline distribution is randomized at scales greater than 50 m. This is a clear indication that dolines define alignments along the major fracture direction within ±25 m. Since this 50-m width corresponds to a reasonable width for fracture zones in this area, it suggests that the shear zone associated with faulting

promotes doline formation. Applying the same method to larger strips enables the detection of a second level of linear organization of dolines, which is composed of kilometer-wide strips along an average N 120° direction. Three strips are clearly evidenced in the south-eastern part of the L=50 and L=250 m maps of Figure 5. They are cross-cut by two low-density zones, which correspond to the Kué Aval River and to a topographic slope break between two flat areas of the same watershed, both features oriented N 135°. Since dolines only develop on flat areas, none of them are observed on these two zones. Therefore, it is concluded that the kilometer-wide high-density strips are not controlled by any concentration of fractures but rather by topography, according to parameters already evidenced by the PCA.

Toward a typology of dolines in southern New Caledonia

Field surveys allowed five different morphological types of dolines to be recognized. Small objects bounded by steep ferricrete walls appear as collapse features and some can cross-cut road-tracks no older than a few tens of years (Figure 12a). Bowl-shaped objects

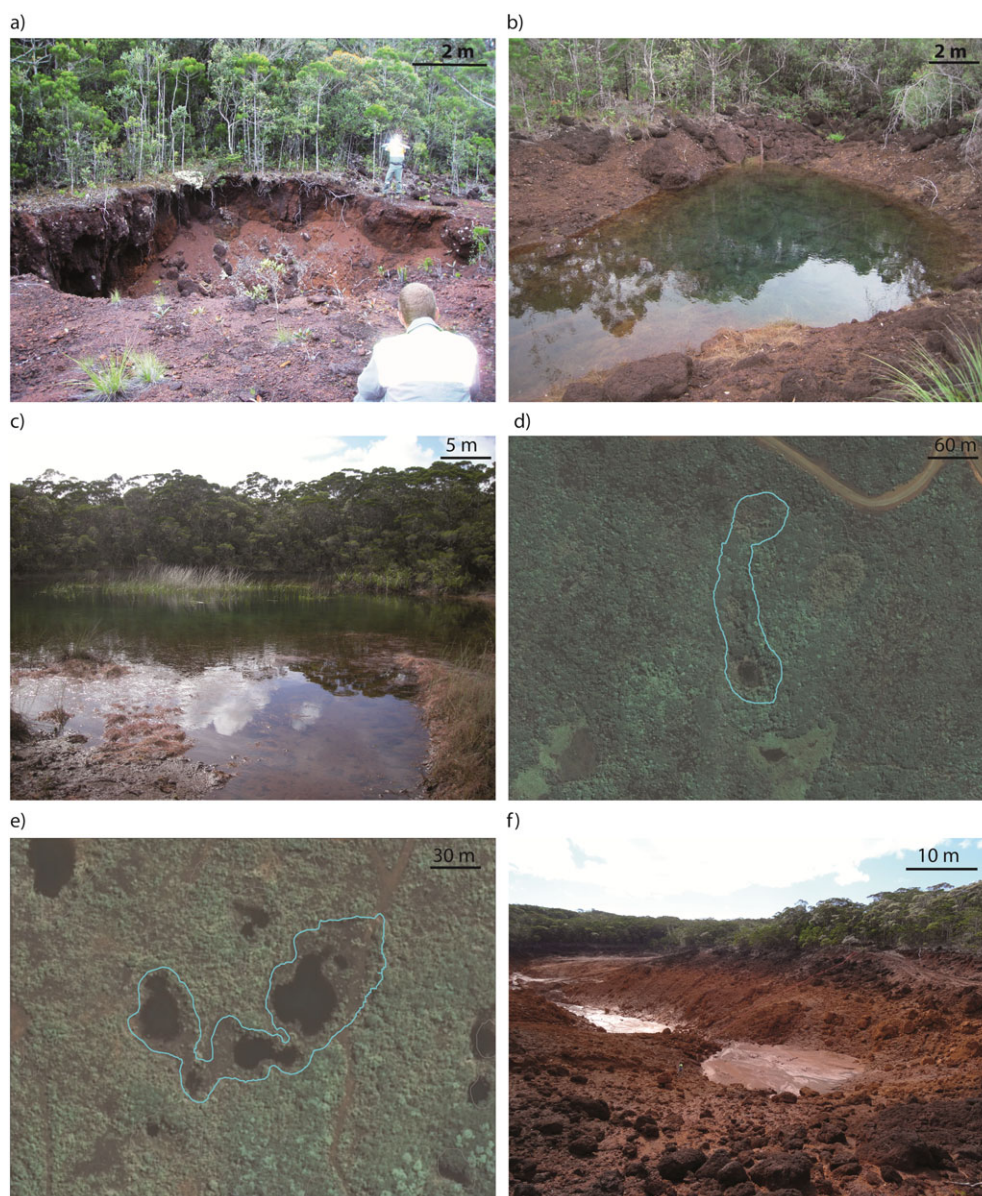


Figure 12. Doline typology based on field observations and DTM analysis: (a) recent collapse; (b) bowl-shaped; (c) flat bottom; (d) and (e) coalescent objects; (f) the Trou du Tahitien.

(Figure 12b) present similar morphology with a larger extension and smoother walls. Flat bottom dolines (Figure 12c), characterized by wetland vegetation and sedimentation, are most commonly observed; several of them appear to be the result of coalescence of at least two closed depressions (Figures 12d and 12e) which could correspond to the elongated objects detected in the previous section (Figure 4). Finally, only one object, the Trou du Tahitien (Figure 12f) is more than 25 m deep; its bottom reaches the base of the weathering profile, and it is known to undergo fast water level fluctuations.

From these field observations, an automatic classification of dolines from LiDAR data is proposed. The mean slope of dolines is used. Collapse dolines are defined by a mean slope steeper than 30° (Salomon, 2000), while the mean slope of bowl-shaped dolines is comprised between 15° and 30° . Other objects, presenting mean slopes lower than 15° are termed as flat bottom. Among them, a threshold value of 10 m is considered for their equivalent diameter. All objects above these threshold values have sediment deposits at their bottom; the largest ones result from coalescence of several dolines. Below the 10 m threshold, dolines present various shapes and sediment infill. The proposed typology defines 36 collapse dolines, 605 bowl-shaped, 5618 small flat bottom and 2342 large flat bottom dolines (Figure 13). Flooded dolines could be abusively included into the flat bottom doline type but field observations reveal that most are actually shallow.

Possible mechanisms involved in the formation and evolution of dolines

The formation of dolines requires a mechanical instability process generating collapse of the ferricrete overlying lateritic

profile. Rainwater infiltrating through ferricrete is trapped at its lower boundary with semi-pervious laterites and forms a superficial perched aquifer, as well as surface runoff when infiltration capacity of the aquifer is exceeded. Void generation at the base of ferricrete is therefore a result of a combination of chemical erosion at the base of the lateritic layer and mechanical erosion at its top (Genna *et al.*, 2005b). Moreover, pervasive circulation of water through the laterite layer may transport fine particles downward by eluviation, thus enhancing the volume reduction associated with dissolution, widening existing joints and leading to suffosion dolines. Eluviation phenomena are also known to produce gullies (Wells and Andriamihaja, 1993), widespread throughout New Caledonia.

The mechanisms involved in the enlargement of dolines are not however clearly understood. We are not able to detect any generation of secondary dolines except near the Trou du Tahitien. Therefore flow focusing toward a main doline should not be a significant parameter for doline generation except for the largest ones. The similarity between the general size distribution of lakes and that observed for dolines indicates that margin erosion and sedimentation play a significant role in doline enlargement. However, these two mechanisms cannot contribute to doline deepening (indeed, they counteract deepening). Doline growth by dissolution of the underlying protolith requires that water arriving in the doline is conveyed through the semi-pervious laterite layer toward the dissolution front. A limited number of pipes can be observed near the lowest point of dolines. Moreover, stability of pipes in a non-cohesive material such as laterite can be questioned.

Bowl-shaped and collapse dolines are anchored to the weathering profile and connected to the hydrogeological system; therefore it is proposed that they are representative of

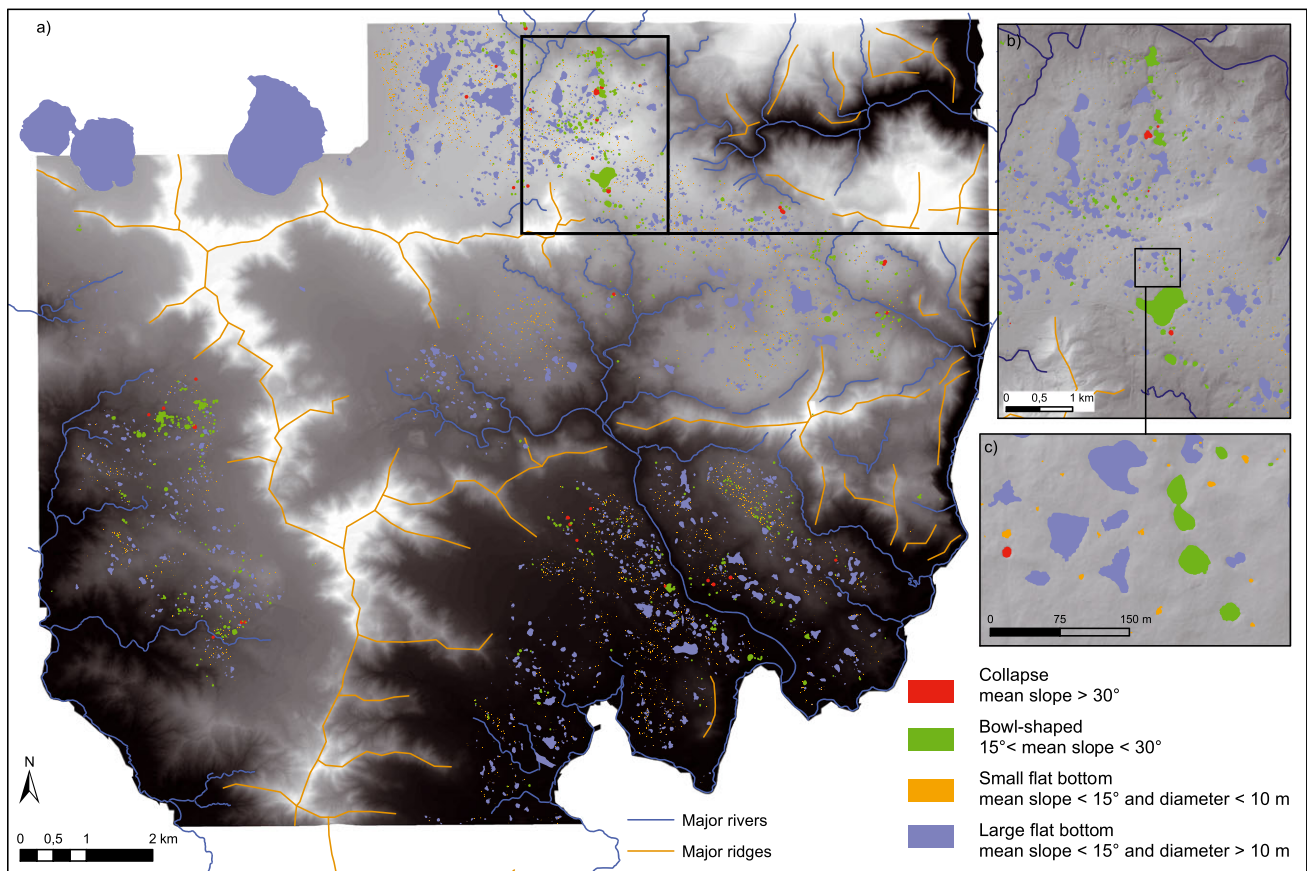


Figure 13. Map of dolines by morphometric types: (a) study area. Collapse and bowl-shaped dolines are slightly expanded (buffer 20 m and 10 m respectively) for better visibility; (b) and (c) enlargements of the Trou du Tahitien area.

an active pseudokarst. By contrast, large flat bottom objects are hydraulically disconnected from the hydrosystem by a low permeability sediment layer. They often correspond to coalescence of several dolines. They are related to a former and now inactive pseudokarst. The small flat bottom type encompasses a larger number of different objects, some of which are infilled by sediments, some others being very similar to shallow bowl-shaped dolines. Therefore, the evolution of small flat bottom dolines is uncertain.

Collapse and bowl-shaped dolines are mainly located within two areas (Figure 13a), one of which is a N–S strip near the Trou du Tahitien (Figures 13b and 13c). This is the only known doline where the bottom reaches the base of the weathering profile with complete removal of the upper regolith. It is located at the intersection of two N–S and E–W lineaments, as indicated by its cross-like shape; this may have promoted deep drainage below the doline. However, the Trou du Tahitien constitutes a unique example and the probable general evolution of dolines goes toward a sediment-filled flat type and the merging of several dolines in a larger, more complex shaped one.

Conclusion

Semi-automatic detection from LiDAR data allowed us to build a dataset of 8601 dolines with areas ranging from 1 m² to 2 km², which constitute a unique dataset on ultramafic pseudokarst. Doline density is linked to rainfall, altitude and watershed morphology mainly because flat basins preserve the weathering profile and hence dolines. They are distributed over 50-m wide zones related to tectonic fracture. Depressions smaller than 10 m² present density and alignment statistics similar to those of larger dolines; they should therefore be considered as dolines.

Based on field studies and on statistical analyses, a typology is proposed for dolines in ultramafic rocks that provides important clues as to pseudokarstic activity. Collapse dolines are small and bounded by vertical walls of ferricrete. Bowl-shaped dolines are larger, present smoother walls within ferricrete and saprolite and little or no sediment infill. Both collapse and bowl-shaped dolines are active features which may enlarge and deepen. Flat bottom dolines are bounded by smooth slopes and generally contain partial to complete sediment infill. The largest ones tend to have the general shapes and size of lakes and are therefore thought to be inactive features, inherited from previous pseudokarsts. Smaller flat bottom dolines present various shapes and may be subjected to a more complex evolution. This study demonstrates the karstic origin of dolines in the ultramafic massif of southern New Caledonia. These results provide a framework for future management of water resources in this type of formation. However, groundwater flow paths associated with the genesis and the evolution of dolines need to be clarified. Hence, this work could lead up to hydrological monitoring of the bowl-shaped or collapse dolines.

Acknowledgements—The authors thank Vale NC for providing the high accuracy DTM data. B. Robineau is thanked for his constructive remarks. Thanks to Celia Northam of the University of Reunion for her reworking and proofreading of the English. This work was supported by the Center for Technological Research on 'Nickel and its Environment' (Centre National de Recherche Technologique, CNRT 'Nickel et son environnement') within the programs 'Doline diagnosis' (2012–2015) and Hyperk (2013–2016). The authors thank the anonymous reviewers and the Editor for their useful remarks and suggestions for improving the manuscript.

References

- Avias J. 1967. Overthrust structure of the main ultrabasic New Caledonian massives. *Tectonophysics* **4**: 531–541.
- Baldwin SL, Rawling T, Fitzgerald PG. 2007. Thermochronology of the New Caledonian high-pressure terrane: implications for middle Tertiary plate boundary processes in the southwest Pacific. *Geological Society of America Special Papers* **419**: 117–134.
- Basso A, Bruno E, Parise M, Pepe M. 2013. Morphometric analysis of sinkholes in a karst coastal area of southern Apulia (Italy). *Environment and Earth Science* **70**: 2545–2559. DOI:10.1007/s12665-013-2297-z.
- Benichou P, Le Breton O. 1987. Prise en compte de la topographie pour la cartographie des champs pluviométriques statistiques [Use of topography on mapping of statistical rainfall fields]. In *La Météorologie*, 7th Series; 23–34.
- Bogdanov I, Huaman D, Thovet J-F, Genthon P, Adler PM. 2011. Tectonic stresses seaward of an aseismic ridge—trench collision zone. A remote sensing approach on the Loyalty Islands, SW Pacific. *Tectonophysics* **499**: 77–91. DOI:10.1016/j.tecto.2010.12.007.
- Bondesan A, Meneghel M, Sauro U. 1992. Morphometric analysis of dolines. *International Journal of Speleology* **21**: 1–55.
- Cabioch G, Recy J, Jouannic C, Turpin L. 1996. Contrôle climatique et tectonique de l'édification récifale en Nouvelle-Calédonie au cours du Quaternaire terminal. *Bulletin de la Société Géologique de France* **167**: 729–742.
- Chevillotte V, Chardon D, Beauvais A, Maurizot P, Colin F. 2006. Long-term tropical morphogenesis of New Caledonia (Southwest Pacific): importance of positive epeirogeny and climate change. *Geomorphology* **81**: 361–375. DOI:10.1016/j.geomorph.2006.04.020.
- Clark PJ, Evans FC. 1954. Distance to nearest neighbor as a measure of spatial relationships in populations. *Ecology* **35**: 445–453.
- Closson D, Karaki NA. 2009. Salt karst and tectonics: sinkholes development along tension cracks between parallel strike-slip faults, Dead Sea, Jordan. *Earth Surface Processes and Landforms* **34**: 1408–1421. DOI:10.1002/esp.1829.
- Cluzel D, Aitchison JC, Picard C. 2001. Tectonic accretion and underplating of mafic terranes in the Late Eocene intraoceanic fore-arc of New Caledonia (Southwest Pacific): geodynamic implications. *Tectonophysics* **340**: 23–59.
- Cluzel D, Jourdan F, Meffre S, Maurizot P, Lesimple S. 2012a. The metamorphic sole of New Caledonia ophiolite: ⁴⁰Ar/³⁹Ar, U–Pb, and geochemical evidence for subduction inception at a spreading ridge. *Tectonics* **31**. DOI:10.1029/2011TC003085.
- Cluzel D, Maurizot P, Collot J, Sevin B. 2012b. An outline of the geology of New Caledonia; from Permian – Mesozoic Southeast Gondwanaland active margin to Cenozoic obduction and supergene. *Episodes* **35**(1): 72–86.
- Cluzel D, Meffre S, Maurizot P, Crawford AJ. 2006. Earliest Eocene (53 Ma) convergence in the Southwest Pacific: evidence from pre-obduction dikes in the ophiolite of New Caledonia. *Terra Nova* **18**: 395–402. DOI:10.1111/j.1365-3121.2006.00704.x.
- Day M. 1983. Doline morphology and development in Barbados. *Annals of the Association of American Geographers* **73**: 206–219. DOI:10.1111/j.1467-8306.1983.tb01408.x.
- Dewandel B, Lachassagne P, Bourdier F, Al-Hattali S, Ladouche B, Pinault J-L, Al-Suleimani Z. 2005. A conceptual hydrogeological model of ophiolite hard-rock aquifers in Oman based on a multiscale and a multidisciplinary approach. *Hydrogeology Journal* **13**: 708–726. DOI:10.1007/s10040-005-0449-2.
- Dubois J, Launay J, Recy J. 1974. Uplift movements in New Caledonia-Loyalty Islands area and their plate tectonics interpretation. *Tectonophysics* **24**: 133–150.
- Folcher N, Sevin B, Quesnel F, Lignier V, Allenbach M, Maurizot P, Cluzel D. 2015. Neogene terrestrial sediments: a record of the post-obduction history of New Caledonia. *Australian Journal of Earth Sciences* **62**: 479–492. DOI:10.1080/08120099.2015.1049207.
- Ford D, Williams P. 2007. *Karst Hydrogeology and Geomorphology*. John Wiley & Sons: Chichester.
- Freyssinet P, Butt CRM, Morris RC, Piantone P. 2005. Ore-forming processes related to lateritic weathering. *Economic Geology 100th Anniversary* 681–722.
- Fritsch E. 2012. Planche 15: Les sols/Chapitre II: Les milieux. In *Atlas de la Nouvelle-Calédonie*, Bonvallot J, J-C G, Habert E (eds). IRD-Congrès de la Nouvelle-Calédonie: New Caledonia.

- Fritsch E, Juillot E, Dublet G, Fandeur D, Fonteneau L, Martin E, Auzente AL, Morin G, Robert JL, Galois L, Calas G, Grauby O, Boulvais P, Cathelineau M. 2014. Analyse fine de minerais latéritiques (approches pétrographique, minéralogique, géochimique et isotopique), Rapport final 2014. CNRT Noumea, New Calédonia.
- Gabrovsek F, Stepisnik U. 2011. On the formation of collapse dolines: a modelling perspective. *Geomorphology* **134**: 23–31. DOI:10.1016/j.geomorph.2011.06.007.
- Gao Y, Alexander E, Jr, Tipping RG. 2005. Karst database development in Minnesota: design and data assembly. *Environmental Geology* **47**: 1072–1082. DOI:10.1007/s00254-005-1240-3.
- Genna A, Bailly L, Lafoy Y, Augé T. 2005a. Les karsts latéritiques de Nouvelle-Calédonie. *Kardiologia* **45–46**: 19–28.
- Genna A, Maurizot P, Lafoy Y, Augé T. 2005b. Contrôle karstique de minéralisations nickélfères de Nouvelle-Calédonie. *Comptes-Rendus Géoscience* **337**: 367–374.
- Höfle B, Griesbaum L, Forbriger M. 2013. GIS-Based Detection of Gullies in Terrestrial LiDAR Data of the Cerro Llamoca Peatland (Peru). *Remote Sensing* **5**: 5851–5870. DOI:10.3390/rs5115851.
- Jeanpert J. 2010. Hydrogéologie des massifs de péridotites de Nouvelle-Calédonie. Bilan des connaissances et hypothèses de travail. SGNC: 49p Noumea, New Calédonia
- Jeanpert J, Dewandel B. 2013. Analyse préliminaire des données hydrogéologiques d'un massif minier ultrabasique de Nouvelle-Calédonie – SGNC/DIMENC. BRGM/RP-61765-FR, Report.
- Jennings JN. 1975. Doline Morphometry as a Morphogenetic Tool: New Zealand Examples. *New Zealand Geographer* **31**: 6–28. DOI:10.1111/j.1745-7939.1975.tb00793.x.
- Join J-L, Robineau B, Ambrosi J-P, Costis C, Colin F. 2005. Système hydrogéologique d'un massif minier ultrabasique de Nouvelle-Calédonie. *Comptes-Rendus Géoscience* **337**: 9.
- Kemmerly PR. 1976. Definitive doline characteristics in the Clarksville quadrangle, Tennessee. *Geological Society of America Bulletin* **87**: 42–46.
- Kemmerly PR. 1982. Spatial analysis of a karst depression population: clues to genesis. *Geological Society of America Bulletin* **93**: 1078–1086.
- Kobal M, Bertoncelj I, Pirotti F, Dakskobler I, Kutnar L. 2015. Using Lidar data to analyse sinkhole characteristics relevant for understory vegetation under forest cover—case study of a high karst area in the Dinaric Mountains. *PloS One* **10**. DOI:10.1371/journal.pone.0122070.e0122070
- Lagabrielle Y, Maurizot P, Lafoy Y, Cabioch G, Pelletier B, Régnier M, Wabete I, Calmant S. 2005. Post-Eocene extensional tectonics in Southern New Caledonia (SW Pacific): insights from onshore fault analysis and offshore seismic data. *Tectonophysics* **403**: 1–28.
- Le Corvec N, Spörl KB, Rowland J, Lindsay J. 2013. Spatial distribution and alignments of volcanic centers: clues to the formation of monogenetic volcanic fields. *Earth-Science Reviews* **124**: 96–114. DOI:10.1016/j.earscirev.2013.05.005.
- Legueré J. 1976. Des corrélations entre la tectonique cassante et l'altération supergène des péridotites de Nouvelle-Calédonie, PhD. Thesis. Université des sciences et techniques du Languedoc, Montpellier; 80.
- Leou Tham O. 2005. Etude pour la paramétrisation optimale du modèle AURELHY en Nouvelle-Calédonie. Météo France; 14 pp. Noumea, New Calédonia
- Lutz T. 1986. An analysis of the orientations of large-scale crustal structures: a statistical approach based on areal distributions of pointlike features. *Journal of Geophysical Research* **91**: 421–434.
- Lyew-Ayee P, Viles H, Tucker G. 2006. The use of GIS-based digital morphometric techniques in the study of cockpit karst. *Earth Surface Processes and Landforms* **32**: 165–179.
- Mandelbrot B. 1983. *The Fractal Geometry of Nature*. Freeman: New York.
- Matsushita M, Ouchi S, Honda K. 1991. On the fractal structure and statistics of contour lines on a self-affine surface. *Journal of the Physical Society of Japan* **60**: 2109–2112. DOI:10.1143/JPSJ.60.1109.
- Maurizot P. 2011. First sedimentary record of the pre-obduction convergence in New Caledonia: formation of an Early Eocene accretionary complex in the north of Grande Terre and emplacement of the 'Montagnes Blanches' nappe. *Bulletin de la Société Géologique de France* **182**: 479–491. DOI:10.2113/gssgfbull.182.6.479.
- Maurizot P. 2013. Palaeocene age for the Adio Limestone, New Caledonia: stratigraphic and regional context. *New Zealand Journal of Geology and Geophysics* **56**: 16–26. DOI:10.1080/00288306.2012.735677.
- Maurizot P, Cluzel D. 2014. Pre-obduction records of Eocene foreland basins in central New Caledonia: an appraisal from surface geology and Cadart-1 borehole data. *New Zealand Journal of Geology and Geophysics* **57**: 300–311. DOI:10.1080/00288306.2014.885065.
- de la Rosa J MI. 2012. Chapter: 3.6.1. Karst landform classification techniques. In *Geomorphological Techniques*, Clarke L (ed). British Society for Geomorphology: London.
- Mendonça A, Pires A, Barros J. 1994. Pseudosinkhole occurrences in Brasília, Brazil. *Environmental Geology* **23**: 36–40.
- Météo France. 2007. Atlas climatique de la Nouvelle-Calédonie. Météo France; 128 pp. Noumea, New Calédonia
- Milanovic PT. 2004. *Water Resources Engineering in Karst*. In Taylor & Francis Group. CRC Press: London.
- Moutte J, Paris J. 1976. Anatomy and structure of the great southern massif (New Caledonia). In *International Symposium on Geodynamics in South-West Pacific*, Noumea; 229–234.
- Obu J, Podobnikar T. 2013. Algoritem za prepoznavanje kraških kotanj na podlagi digitalnega modela reliefa [Algorithm for karst depression recognition using digital terrain model]. *Geodetski Vestnik* **57**: 260–270.
- Pardo-Iguzquiza E, Duran JJ, Dowd PA. 2013. Automatic detection and delineation of karst terrain depressions and its application in geomorphological mapping and morphometric analysis. *Acta Cardiologica* **42**: 17–24.
- Prinzhofer A, Nicolas A, Cassard D, Moutte J, Leblanc M, Paris JP, Rabinovitch M. 1980. Structures in the New Caledonia peridotites-gabbros: Implications for oceanic mantle and crust. *Tectonophysics* **69**: 85–112. DOI:10.1016/0040-1951(80)90128-6.
- Robineau B, Join J-L. 2005. Tectonique et microtectonique cassante du massif de Tiébaghi. Géométrie des sillons d'altération sous cuirasse imagée par la Tomographie de Résistivité Electrique. IRD - UR Nouméa, New Caledonia
- Robineau B, Join J-L, Beauvais A, Parisot J-C, Savin C. 2007. Geoelectrical imaging of a thick regolith developed on ultramafic rocks: groundwater influence. *Australian Journal of Earth Sciences* **54**: 773–781. DOI:10.1080/08120090701305277.
- Salomon J-N. 2000. Précis de karstologie. Presses universitaires de Bordeaux
- Seekell DA, Pace ML, Tranvik LJ, Verpoorter C. 2013. A fractal-based approach to lake size-distributions. *Geophysical Research Letters* **40**: 1–5. DOI:10.1002/grl.50139.
- Segura FS, Pardo-Pascual JE, Rossello VM, Fornos JJ, Gelabert B. 2007. Morphometric indices as indicators of tectonic, fluvial and karst processes in calcareous drainage basins, South Menorca Island, Spain. *Earth Surface Processes and Landforms* **32**: 1928–1946. DOI:10.1002/esp.1506.
- Sevin B. 2014. Cartographie du régolithe sur formation ultrabasique de Nouvelle-Calédonie: localisation dans l'espace et le temps des gisements nickélfères, PhD Thesis. Université de Nouvelle-Calédonie; 402 pp.
- Sevin B, Cluzel D, Maurizot P, Ricordel-Prognon C, Chaproniere G, Folcher N, Quesnel F. 2014. A drastic lower Miocene regolith evolution triggered by post obduction slab break-off and uplift in New Caledonia. *Tectonics* **33**: 15. DOI:10.1002/2014TC003588.
- Sevin B, Maurizot P, Vendé-Leclerc M. 2012a. Carte géologique du Grand Sud de Nouvelle-Calédonie au 1/50 000. Service Géologique de la Nouvelle-Calédonie – Bureau de Recherches Géologiques et Minières Noumea, New Calédonia.
- Sevin B, Ricordel-Prognon C, Quesnel F, Cluzel D, Lesimple S, Maurizot P. 2012b. First paleomagnetic dating of ferricrete in New Caledonia: new insight on the morphogenesis and paleoweathering of 'Grande Terre'. *Terra Nova* **24**: 77–85. DOI:10.1111/j.1365-3121.2011.01041.x.
- Shan J, Toth CK. 2008. *Topographic Laser Ranging and Scanning: Principles and Processing*. CRC Press: Boca Raton, FL.
- Siart C, Forbriger M, Nowaczinski E, Hecht S, Höfle B. 2013. Fusion of multi-resolution surface (terrestrial laser scanning) and subsurface geodata (ERT, SRT) for karst landform investigation and geomorphometric quantification. *Earth Surface Processes and Landforms* **38**: 1135–1147. DOI:10.1002/esp.3394.

- Sustersic F. 1994. Classic dolines of classical site. *Acta Cardiologica* **23**: 123–154.
- Telbisz T, Dragusica H, Nagy B. 2009. Doline morphometric analysis and karst morphology of Biokovo Mt (Croatia) based on field observations and digital terrain analysis. *Hrvatski geografski glasnik* **71**(2): 5–22.
- Thomas MF. 1994. *Geomorphology in the Tropics: A Study of Weathering and Denudation in Low Latitudes*. John Wiley & Sons: Chichester.
- Thorne RL, Roberts S, Herrington R. 2012. Climate change and the formation of nickel laterite deposits. *Geology* **40**: 331–334. DOI:10.1130/g32549.1.
- Titus SJ, Maes SM, Benford B, Ferre EC, Tikoff B. 2011. Fabric development in the mantle section of a paleotransform fault and its effect on ophiolite obduction, New Caledonia. *Lithosphere* **3**: 221–244. DOI:10.1130/l122.1.
- Trescases J-J. 1975. L'évolution géologique supergène des roches ultrabasiqes en zone tropicale. Formation des gisements nickélicifères de Nouvelle-Calédonie. *Mémoire ORSTOM* **78**: 1–259.
- Ulrich M, Picard C, Guillot S, Chauvel C, Cluzel D, Meffre S. 2010. Multiple melting stages and refertilisation process as indicators for ridge to subduction formation: the New Caledonia Ophiolite. *Lithos* **115**: 223–236.
- Vosselman GV, Maas H-G. 2010. *Airborne and Terrestrial Laser Scanning*. Whittles: Caithness.
- Waltham AC, Fookes PG. 2003. Engineering classification of karst ground conditions. *Quarterly Journal of Engineering Geology and Hydrogeology* **36**: 101–118 .DOI. 1470-9236/03
- Wand MP, Jones MC. 1995. *Kernel Smoothing*. Chapman and Hall: London.
- Wells N, Andriamihaja B. 1993. The initiation and growth of gullies in Madagascar: are humans to blame? *Geomorphology* **8**: 1–46.